Interpretation of Fracture Toughness and *R*-Curve Behavior by Direct Observation of Microfracture Process in Ti-Based Dendrite-Containing Amorphous Alloys

CHANGWOO JEON, CHOONGNYUN PAUL KIM, HYOUNG SEOP KIM, and SUNGHAK LEE

Fracture properties of Ti-based amorphous alloys containing ductile β dendrites were explained by directly observing microfracture processes. Three Ti-based amorphous alloys were fabricated by adding Ti, Zr, V, Ni, Al, and Be into a Ti-6Al-4V alloy by a vacuum arc melting method. The effective sizes of dendrites varied from 63 to 104 μm, while their volume fractions were almost constant within the range from 74 to 76 pct. The observation of the microfracture of the alloy containing coarse dendrites revealed that a microcrack initiated at the amorphous matrix of the notch tip and propagated along the amorphous matrix. In the alloy containing fine dendrites, the crack propagation was frequently blocked by dendrites, and many deformation bands were formed near or in front of the propagating crack, thereby resulting in a zig-zag fracture path. Crack initiation toughness was almost the same at 35 to 36 MPa$\sqrt{\text{m}}$ within error ranges in the three alloys because it was heavily affected by the stress applied to the specimen at the time of crack initiation at the crack tip as well as strength levels of the alloys. According to the *R*-curve behavior, however, the best overall fracture properties in the alloy containing fine dendrites were explained by mechanisms of blocking of the crack growth and crack blunting and deformation band formation at dendrites.

DOI: 10.1007/s11661-015-2743-5

I. INTRODUCTION

ADVANCES in bulk amorphous alloys have been remarkably made by developing amorphous alloys with high glass-forming ability.[1–6] However, there are problems that remain to be solved, typical one of which is brittle fracture. When amorphous alloys are externally loaded, shear bands play an important role in initiating the fracture, leading to abrupt shear fracture.[7,8] In order to overcome this problem of brittle fracture, the developmental activities on composite-type alloys by homogeneously distributing ductile crystalline particles in an amorphous matrix have been performed.[9–11] In the recently developed Zr- and Ti-based amorphous alloys, where ductile dendrites are formed *in situ* from the amorphous alloy melt, the ductility is greatly enhanced by forming a number of deformation bands at dendrites.[10–15]

According to Hofmann *et al.*,[12] the tensile strength and ductility were increased to 1510 MPa and 9.5 pct, respectively, by increasing the volume fraction of dendrite to 47 pct in Zr-based amorphous alloys containing more Ti content (31 to 34 at. pct) than that in a conventional Zr-based amorphous alloy containing dendrites (*i.e.*, an 'LM2' alloy (commercial brand name of the Liquidmetal Technologies, Lake Forest, CA)). In some Ti-based amorphous alloys, whose volume fraction of dendrite was higher than 70 pct, the tensile ductility reached 10 pct.[13] In order to further enhance the tensile ductility, together with crack initiation and growth toughness, the size and volume fraction of dendrite should be optimized. Systematic understanding of the correlation between microstructure and fracture toughness is also required for the accurate evaluation of fracture toughness, and microfracture mechanisms should be verified in relation with microstructure. A simple way for examining microfracture mechanisms is an observation of fractured surfaces, which can lead to effectively explaining the crack initiation and growth toughness. Studies on detailed fracture mechanisms such as direct observation of crack initiation and propagation processes[16,17] or deformed microstructures beneath the fractured surfaces[18,19] have also been conducted. In spite of these efforts, many difficulties still remain to be addressed to correlate microscopic fracture mechanisms with macroscopic fracture toughness.

In this study, crack initiation toughness of Ti-based amorphous alloys was measured, and mechanisms related with improvement of crack initiation and growth toughness were examined by direct observation of microfracture processes. Three Ti-based amorphous alloys containing ductile dendrites were fabricated by adding alloying elements of Ti, Zr, V, Ni, Al, and Be

CHANGWOO JEON, Postdoctoral Research Associate, and CHOONGNYUN PAUL KIM, Research Professor, are with the Center for Advanced Aerospace Materials, Pohang University of Science and Technology, Pohang 790-784, Korea. HYOUNG SEOP KIM and SUNGHAK LEE, Professors, are with the Center for Advanced Aerospace Materials, Pohang University of Science and Technology, and also with the Materials Science and Engineering, Pohang University of Science and Technology, Pohang 790-784, Korea. Contact e-mail: shlee@postech.ac.kr
Manuscript submitted August 15, 2014.
Article published online January 16, 2015

into a conventional Ti-6Al-4V alloy. The Ti-Zr-V-Ni-Al-Be alloy system is originated from Hofmann *et al.*,[20] but our alloy design concept was focused on economic fabrication of Ti-based amorphous alloys and simultaneous improvement of ductility and crack initiation and growth toughness.[21] Microfracture processes were directly observed by using an *in situ* loading stage installed inside a scanning electron microscope (SEM) chamber, and microfracture mechanisms were investigated by focusing on how dendrites affect the initiation and propagation of cracks.[22–25] This experiment enabled us to examine the crack initiation and propagation behavior occurring at a sharp notch tip and to study the *R*-curve behavior in which the fracture resistance increases with the crack growth.[26,27]

II. EXPERIMENTAL

Three Ti-based amorphous alloys were designed by adding Ti, Zr, V, Ni, Al, and Be into a Ti-6Al-4V alloy (composition: Ti-6Al-4V-0.1O-0.02N-0.04C (wt pct)). They were basically originated from the Ti-Zr-V-Ni-Al-Be system of Hofmann *et al.*,[20] but the content of Al was somewhat higher than the original Ti-Zr-V-Ni-Al-Be system because of the utilization of commercial Ti-6Al-4V alloy. The weight percent of the Ti-6Al-4V alloy was 18 pct (20 at. pct), and the amounts of addition of Ti, Zr, V, Ni, Al, and Be into the Ti-6Al-4V alloy were varied to achieve the overall chemical compositions as shown in Table I. Dendrites of β phase (bcc structure) are well formed when the amount of (Ti + Zr) exceeds 70 at. pct,[14,15] and V and Al generally work as stabilizers of β and α phases, respectively, in Ti alloys.[28] The amount of V is relatively high to obtain sufficient dendrites of β phase in the current alloy system.[15,29] Ni and Be are known to improve the amorphous-forming ability.[13–15] The D1 alloy has the basic composition of the Ti-Zr-V-Ni-Al-Be alloy, and the D2 and D3 alloys have the smaller amounts of Al and Be than that of the D1 alloy. The alloys were fabricated by a vacuum arc melting method under an argon atmosphere, held at temperatures ranging from 1073 K to 1173 K (800 °C to 900 °C) for 30 minutes, and quenched to room temperature.

The alloys were polished in diamond pastes (size: 0.25 μm), etched by a solution of 40 mL HF, 20 mL HNO_3, 40 mL HCl, and 200 mL H_20, and observed on an SEM (model; JSM-6330F, Jeol, Japan). The average size and volume fraction of dendrites were measured by an image analyzer. Overall bulk hardness of the alloys and microhardness of dendrite were measured by a Vickers hardness tester under 500 and 5 g loads, respectively. Electron backscatter diffraction (EBSD) analysis (step size; 0.1 μm) was conducted by a field emission scanning electron microscope (FE-SEM, model; Helios Nanolab™, FEI). The data were then interpreted by orientation imaging microscopy (OIM) analysis software provided by TexSEM Laboratories, Inc. The alloys were machined into plate-type tensile specimens of 1 × 2.5 × 6.4 mm in the gage section size, and room-temperature tensile tests were conducted on these specimens at a strain rate of 5.2×10^{-4} s^{-1} by a universal testing machine (model; 8862, Instron Corp., Canton, MA) with capacity of 10,000 kg.

A tension-type loading stage was installed inside an SEM, on which a thin compact tension (CT) specimen with a thickness of 0.5 mm in the grooved section was placed to conduct the *in situ* SEM fracture tests (Figures 1(a) and (b)).[30] According to Lewandowski *et al.*,[31] the fracture toughness increased with the increasing notch root radius, and the effects of notch root radius were larger in bulk amorphous alloys than those in crystalline materials. In addition, the effects of notch root radius in Zr-based bulk amorphous alloys were working even at very small notch root radius of 20 μm.[32] Considering this notch root radius sensitivity, a sharp notch of 20 μm or smaller in root radius should be introduced into the CT specimen, but a sharp notch with a radius ranging from about 30 to 40 μm was inserted by an electric discharge machine, considering the difficulty to introduce a fatigue crack due to the brittle nature of the amorphous alloys. The load applied to the specimen was continuously measured by a small-scale load cell (maximum load; 50 kg) installed in the stage, and was recorded on an *X*–*Y* recorder to obtain the load–time curve, from which the maximum load, P_{max}, was determined as P_Q. Here, P_{max} could be used as P_Q in brittle materials.[33] During observation of the specimen surface displayed on an SEM screen, a crack initiated and propagated from the notch tip above a certain stress intensity factor level. These tests were conducted on three CT specimens for each alloy, and a specimen showing typical deformation and fracture behavior was selected for direct observation of microprocess and *R*-curve analysis.

III. RESULTS

A. *Microstructure and Tensile Properties*

Figures 2(a) through (c) are SEM micrographs of the D1, D2, and D3 alloys. Dendritic structures are

Table I. Chemical Compositions of the Ti-Based Amorphous Alloys Modified from a Ti-6Al-4V Alloy[21] (Weight Percent)

Alloy	Ti-6Al-4V	Ti	Zr	V	Ni	Al	Be
D1	18	37.1	29.9	9	3.5	0.5	2
	*	53.7	29.9	9.8	3.5	1.1	2
D2	18	37.4	30	9	3.5	0.3	1.8
	*	53.9	30	9.9	3.5	0.9	1.8
D3	18	37.7	30.2	9	3.5	0.1	1.5
	*	54.1	30.2	10	3.5	0.75	1.5

*Overall chemical compositions of the Ti-based amorphous alloys.

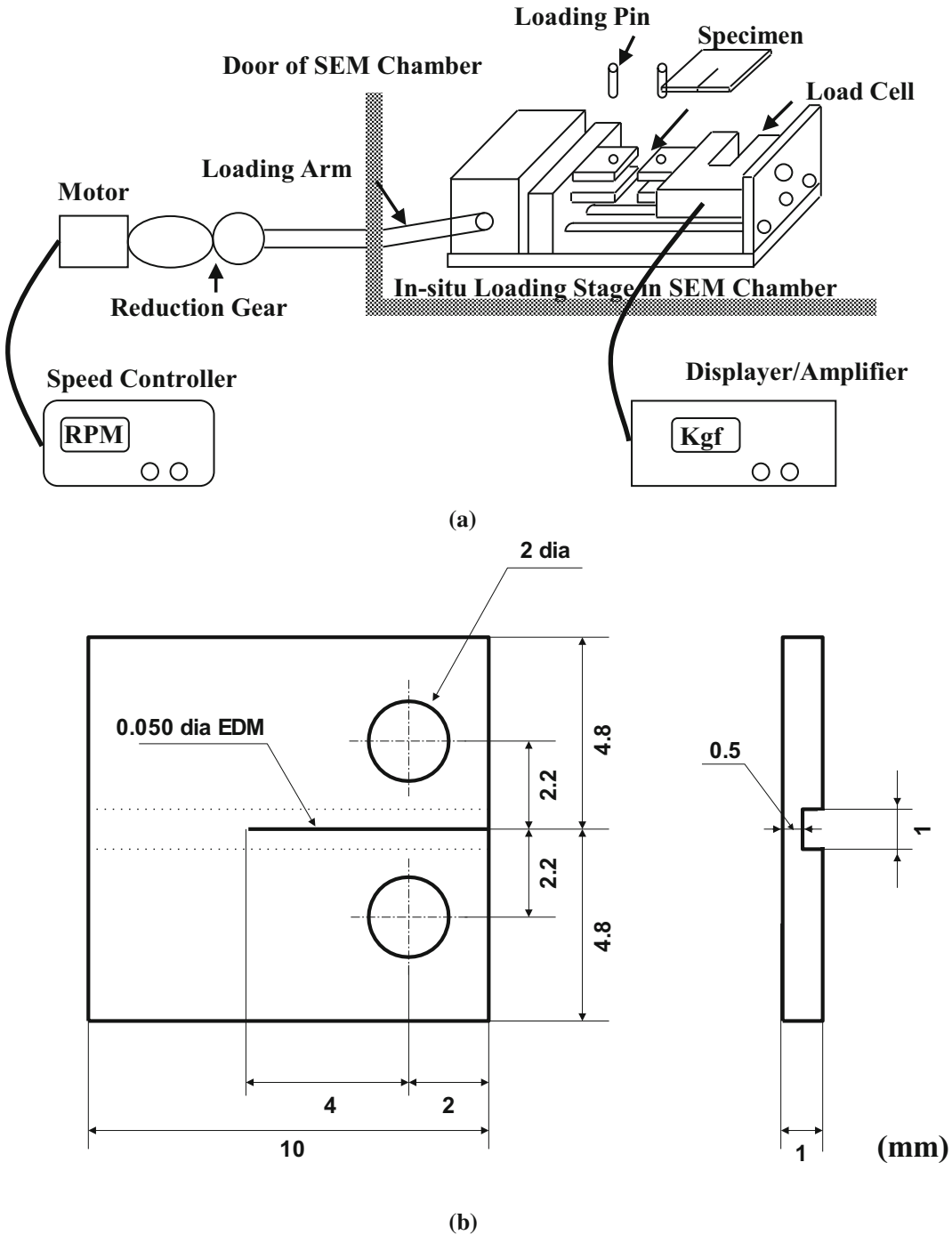

Fig. 1—(*a*) Schematic diagram showing a compact tension (CT)-type loading stage used for *in situ* SEM observation, which was inserted into a vacuum chamber of an SEM. (*b*) Shape and dimensions of a thin CT specimen with a sharp notch.[30] (unit: mm).

homogeneously distributed in the amorphous matrix. These structures were developed as β phases precipitated directly from the melt.[21] The average volume fraction and size have similar values in the ranges from 74 to 76 pct and 24 to 28 μm, respectively, in the three alloys, although they tend to slightly increase in the order of the D1, D2, and D3 alloys since the contents of Al and Be decrease.[21] Figures 3(a) through (c) show the EBSD analysis results of the alloys. Inverse pole figure (IPF) color maps can be represented in different colors, depending on the orientation of each point. In other words, dendrites having the same orientation are represented in the same color. For this reason, the size of dendrites having the same color which are measured by IPF color maps can be considered effective size of dendrites. The sizes of dendrites shown in Figures 2(a) through (c) are estimated to be roughly 24 to 28 μm, but the actual effective sizes shown in Figures 3(a) through (c) are much larger because dendrites having similar or the same orientations are three-dimensionally interconnected.

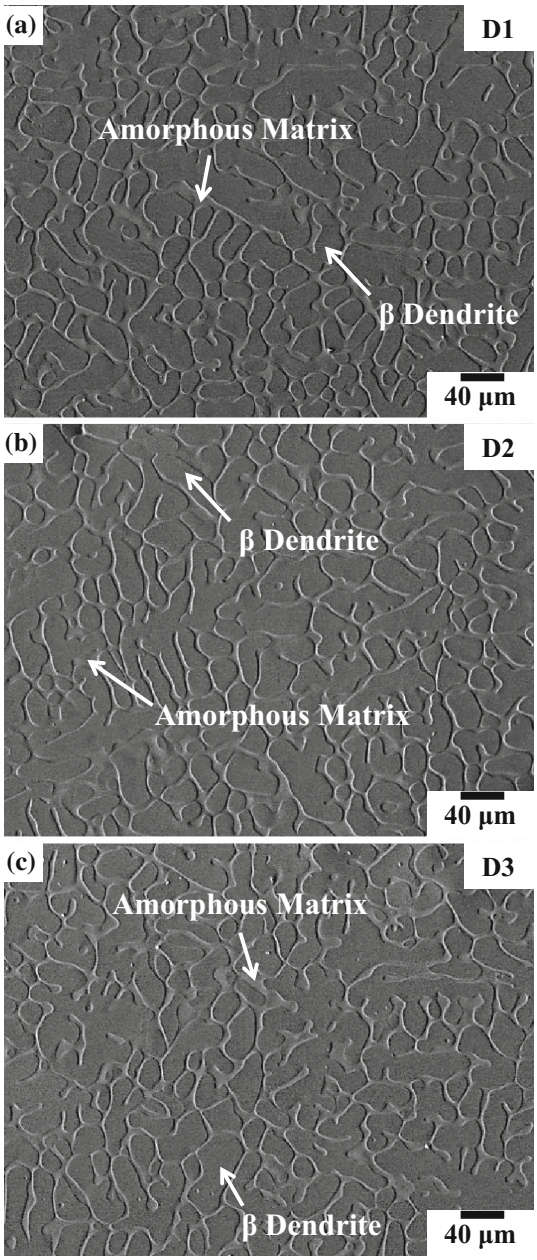

Fig. 2—SEM micrographs of the (*a*) D1, (*b*) D2, and (*c*) D3 alloys. Ductile dendrites are distributed in the amorphous matrix. The average volume fraction and size are similar at 74 to 76 pct and 24 to 28 μm, respectively, in the three alloys.

The effective dendrite sizes measured from the IPF maps are 104, 81, and 63 μm for the D1, D2, and D3 alloys, respectively.[21]

Table II shows the Vickers hardness test results of the three alloys. The overall bulk hardness decreases in the order of the D1, D2, and D3 alloy. This hardness trend is associated with the hardness of dendrite, which is the lowest in the D3 alloy. The room-temperature tensile test results are shown in Table II.[21] The yield, and the tensile strengths and the elongation of the D1 alloy are 1394 MPa, 1485 MPa, and 3.2 pct, respectively, and the D2 alloy has the higher yield and tensile strengths and elongation than the D1 alloy. The D3 alloy has the lower strengths and the higher elongation than those of the D2 alloy. The yield and tensile strengths do not vary much with values in the ranges of 1390 to 1440 and 1490 to 1510 MPa, respectively, but the tensile elongation clearly increases in the order of the D1, D2, and D3 alloys.

B. *Observation of Microfracture Processes*

Figures 4(a) through (d) provide the SEM micrographs serially showing the fracture processes of the D1 alloy containing coarse dendrites. When a load is applied (stress intensity factor, K_I = 36 MPa$\sqrt{m}$), a microcrack initiates at the amorphous matrix of the notch tip as marked by an arrow in Figure 4(a). Under a high stress intensity factor (K_I = 37 MPa$\sqrt{m}$), the microcrack propagates a little further along the amorphous matrix (Figure 4(b)). Deformation bands are not found even at dendrites. When the stress intensity factor increases further, the crack initiated at the notch tip and abruptly propagated through the CT specimen. Figure 4(c) shows a final crack propagation path along which the main crack propagates relatively linearly as indicated by arrows. At the tip region of the propagated crack, open crack regions are formed in the amorphous matrix areas, and dendrites are deformed between the open crack regions (Figure 4(d)).

Figures 5(a) through (c) provide a series of SEM micrographs showing the fracture processes near a notch tip of the D2 alloy. When the load is applied to the D2 alloy (K_I = 36 MPa$\sqrt{m}$), a microcrack initiates at the notch tip (Figure 5(a)). When the load increases (K_I = 38 MPa$\sqrt{m}$), the microcrack propagates mostly along the amorphous matrix at the notch tip to form a longer crack, while dendrites are not deformed (Figure 5(b)). The crack propagates and then stops to be somewhat blunted when the crack meets with a dendrite as marked by an arrow. Under the higher stress intensity factor of 41 MPa$\sqrt{m}$, the stopped crack starts to rapidly propagate through the CT specimen (Figure 5(c)). The overall crack propagation path has a linear pattern with some fluctuation.

Figures 6(a) through (e) show the fracture processes of the D3 alloy containing small effective dendrites of 63 μm in size. Once the load is applied (K_I = 35 MPa$\sqrt{m}$), deformation bands are formed at dendrites near the notch tip as marked by arrows in Figure 6(a). When the stress intensity factor increases to 38 MPa$\sqrt{m}$, a crack initiates along the amorphous matrix (as indicated by a dotted line in Figure 6(a)) in front of the notch tip (Figure 6(b)). The crack stops to propagate at a dendrite (as marked by an arrow), and deformation bands are well developed in front of the crack tip. Deformation band areas are also expanded to dendrites, which are far away from the notch tip. When the stress intensity factor increases to 43 MPa$\sqrt{m}$, the crack connects with the notch tip, propagates further, and stops when it meets with another dendrite (Figure 6(c)). Another crack is initiated in front of the propagated main crack (as marked by an arrow). This crack is connected with the main crack under the higher stress intensity factor of 45 MPa$\sqrt{m}$ to make a zig-zag fracture path. The crack propagation path is shown in Figure 6(d) (K_I = 45 MPa$\sqrt{m}$). The overall

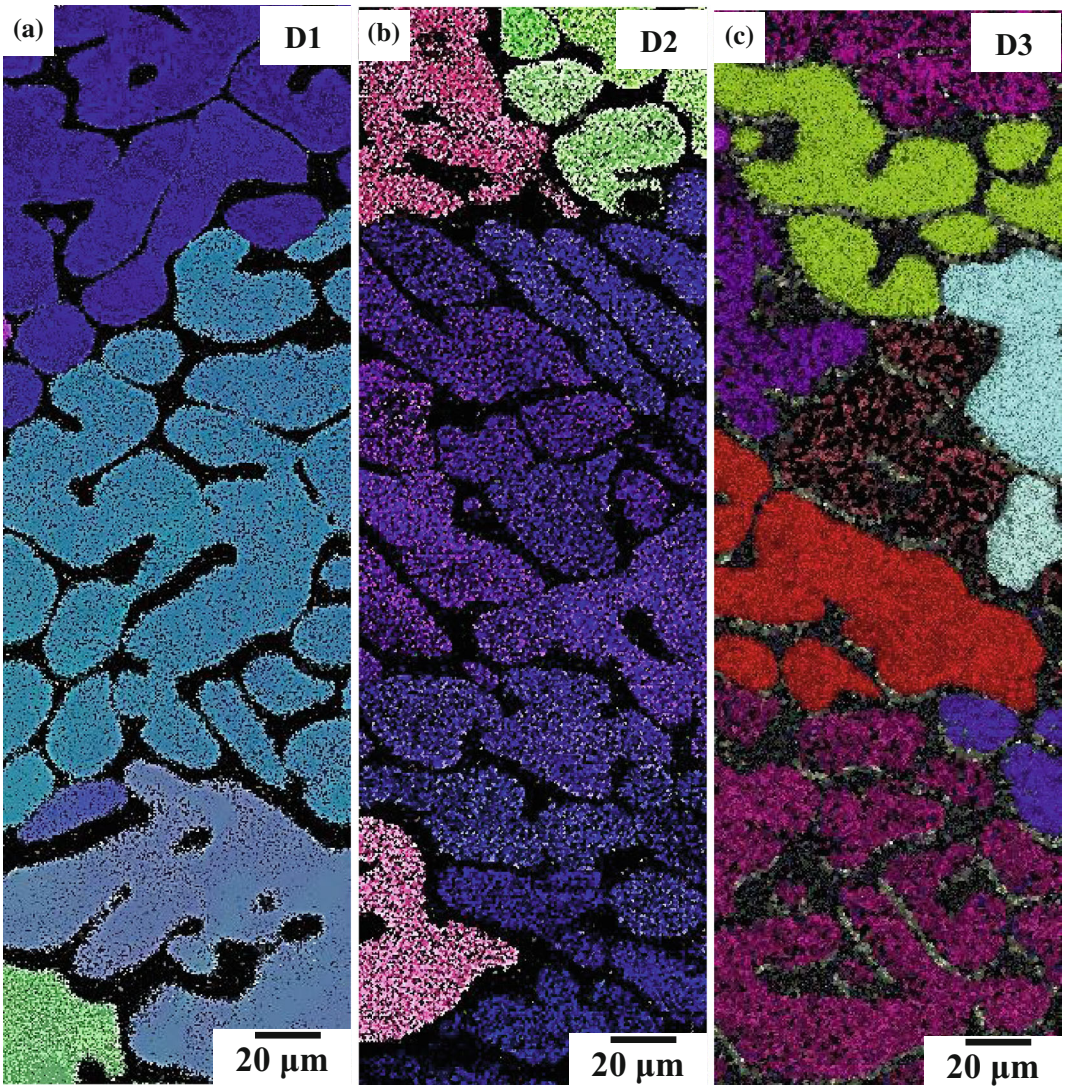

Fig. 3—Inverse pole figure (IPF) color maps of the (*a*) D1, (*b*) D2, and (*c*) D3 alloys. The effective dendrite sizes measured from the IPF maps are 104, 81, and 63 μm for the D1, D2, and D3 alloys, respectively (Color figure online).

Table II. Hardness and Tensile Test Results of the Ti-Based Amorphous Alloys[21]

Alloy	Overall Bulk Hardness (VHN)	Hardness of Dendrite (VHN)	Yield Strength (MPa)	Ultimate Tensile Strength (MPa)	Elongation (pct)
D1	395 ± 10	342 ± 10	1394 ± 70	1485 ± 78	3.2 ± 0.8
D2	374 ± 13	343 ± 10	1443 ± 42	1511 ± 56	5.2 ± 0.2
D3	364 ± 9	331 ± 7	1409 ± 32	1498 ± 15	7.1 ± 0.6

crack propagation path has a curved zig-zag pattern. Figure 6(e) shows an SEM micrograph of the deformed area adjacent to the main crack tip. A number of deformation bands are well developed at dendrites, while multiple shear bands are formed at the amorphous matrix areas.

C. *Crack Initiation Toughness and R-Curve Behavior*

The crack initiation toughness was measured during the course of the *in situ* fracture test. Because a sharp notch (notch tip radius: about 30 to 40 μm) was introduced instead of a fatigue crack, and because thin CT specimens were used in measuring the fracture toughness, toughness values do not satisfy the plane strain condition. In brittle materials like amorphous alloys, however, the fracture toughness measured under the plane stress condition does not deviate much from that measured under the plane strain condition.[33] The crack initiation toughness is obtained from the stress intensity factor measured at the point of the crack initiation in front of the notch tip. The values obtained

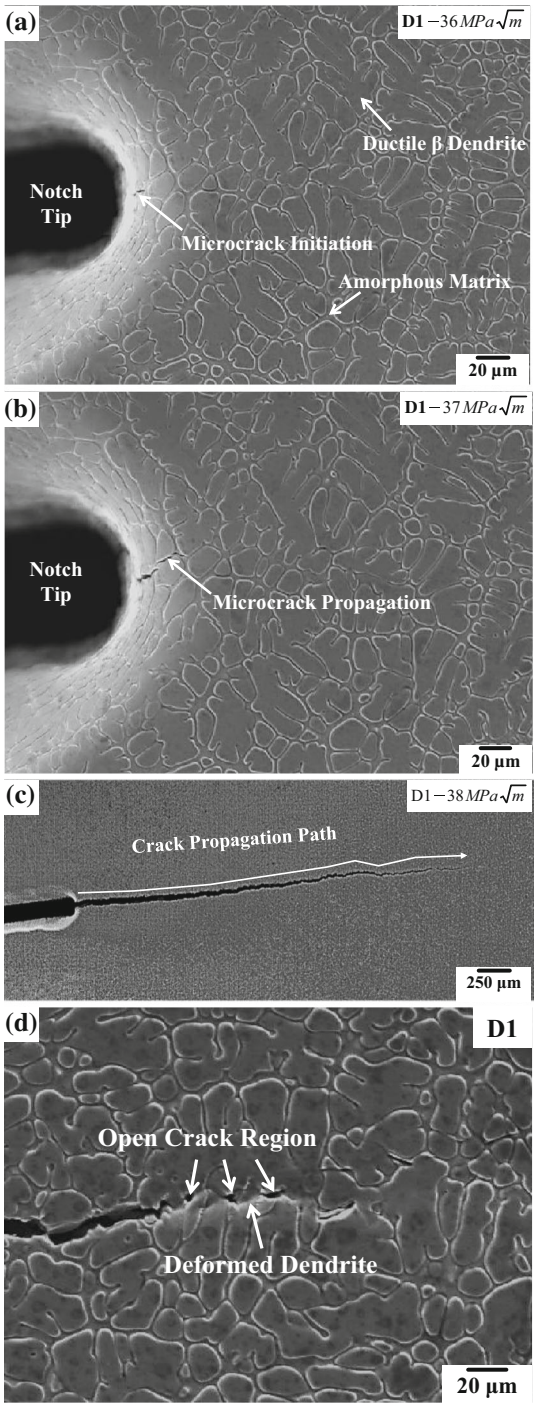

Fig. 4—A series of SEM micrographs near a notch tip of the D1 alloy containing coarse dendrites, showing (*a*) microcrack initiation at the amorphous matrix of the notch tip (K_I = 36 MPa√m), (*b*) microcrack propagation along the amorphous matrix (K_I = 37 MPa√m), (*c*) final crack propagation path (K_I = 38 MPa√m), and (*d*) formation of microvoids and deformation bands at dendrites between the microvoids at the tip region of the propagated crack.

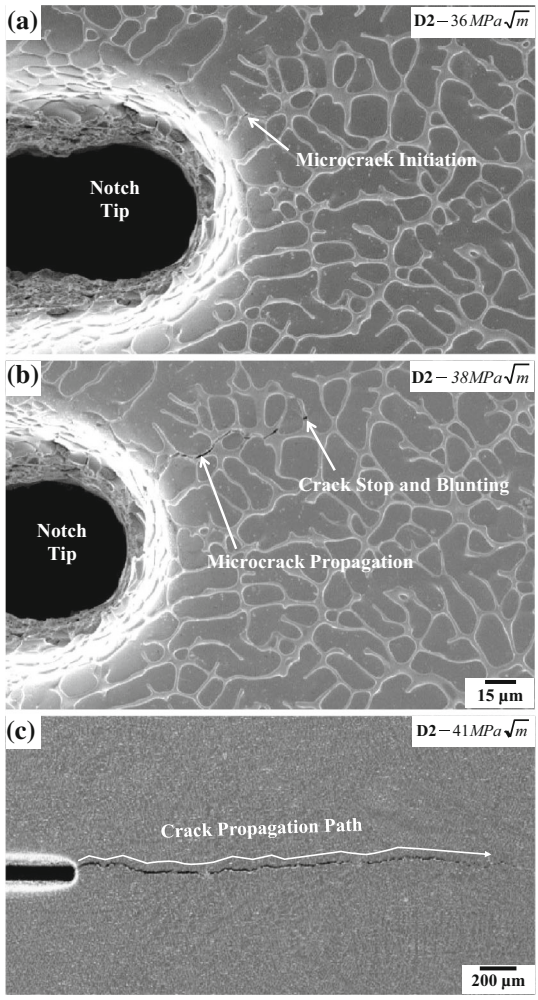

Fig. 5—A series of SEM micrographs near a notch tip of the D2 alloy, showing (*a*) microcrack initiation at the amorphous matrix of the notch tip (K_I = 36 MPa√m), (*b*) microcrack propagation along the amorphous matrix and stop of crack propagation at dendrites (K_I = 38 MPa√m), and (*c*) final crack propagation path (K_I = 41 MPa√m).

are 36, 36, and 35 MPa√m in the D1, D2, and D3 alloys, respectively, which indicates that the crack initiation toughness values are almost the same in the three alloys within error ranges. These crack initiation toughness values are lower than those of versions of these alloys without Al (K_{IC}: about 43 MPa√m).[20] This might be because the higher Al content makes the current alloys somewhat more brittle.

Figure 7 shows *R*-curves of the D1, D2, and D3 alloys obtained by plotting both crack growth length and stress intensity factor measured during the *in situ* fracture test. Since the crack is relatively abruptly grown to fracture in the D1 alloy, the *R*-curve of the D1 alloy can be drawn up to the crack growth of about 0.1 mm. The stress intensity factor at the time of crack initiation, *i.e.*, crack initiation toughness, of the D2 alloy is 36 MPa√m, but steadily increases up to 41 MPa√m with the increasing crack length, which shows the *R*-curve behavior. The D3 alloy shows a more stable crack growth as shown in Figures 6(b) through (d) than those of the D1 and D2 alloys, which indicates the higher resistance to crack growth. This increase in resistance to crack growth is attributed to the continuous deformation at the crack tip region as dendrites block the crack propagation and accelerate the formation of deformation bands.

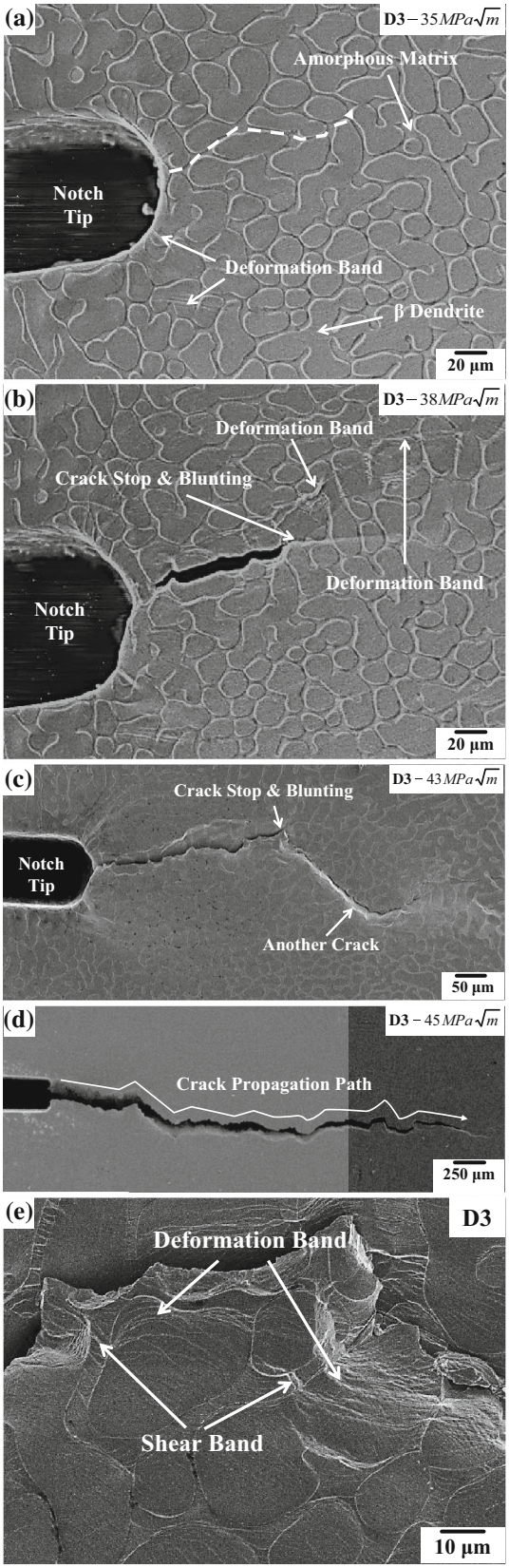

◀ Fig. 6—A series of SEM micrographs near a notch tip of the D3 alloy containing fine dendrites, showing (*a*) formation of deformation bands at dendrites near the notch tip (K_I = 35 MPa√m); (*b*) crack initiation along the amorphous matrix in front of the notch tip, stop of crack propagation at dendrites, and development of deformation bands in front of the crack tip (K_I = 38 MPa√m); (*c*) crack connection with the notch tip and crack propagation and stop at another dendrite (K_I = 43 MPa√m); (*d*) final crack propagation path (K_I = 45 MPa√m); and (*e*) formation of deformation bands at dendrites and multiple shear bands at the amorphous matrix at the tip region of the propagated crack.

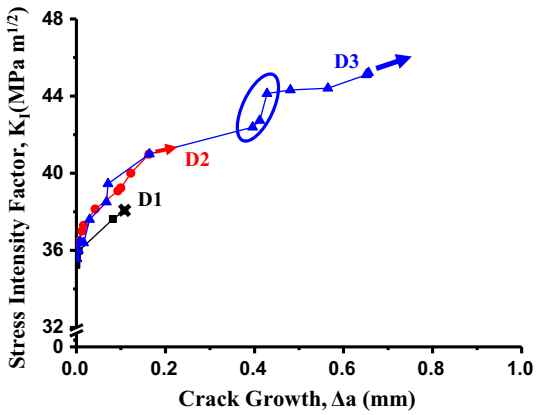

Fig. 7—Fracture resistance curves (*R*-curves) of the D1, D2, and D3 alloys.

IV. DISCUSSION

The current Ti-based amorphous alloys were fabricated by *in situ* formation of ductile dendrites for the improvement purpose of ductility and crack initiation and growth toughness.[12–15] As shown in Table II, the tensile elongation increases in the order of the D1, D2, and D3 alloys, whereas the yield and tensile strengths do not vary much. In addition, the three alloys show the different *R*-curve behaviors in spite of the same crack initiation toughness. In order to explain these results, it is necessary to study the effects of dendrites dispersed in the amorphous matrix on overall fracture properties.

It was confirmed from our previous paper[21] that tensile properties varied with the effective dendrite size. As the effective dendrite size decreases, a number of deformation bands and shear bands are formed along various directions, which prevents the stress concentration and consequently improves the ductility. This formation behavior of deformation bands and shear bands also appears in the current microfracture mechanism study. In the D3 alloy composed of smaller effective dendrites, the crack propagation path of Figure 6(d) shows frequent interruptions in the cracks due to the presence of dendrites, and deformation bands are well developed at dendrites in front of the blunted crack tip (Figure 6(e)). Multiple shear bands are also formed in amorphous matrix areas, as adjacent

dendrites are deformed and connected with the amorphous matrix. Here, dendrites interrupt the crack propagation, act as initiation sites of multiple shear bands, and promote the crack blunting or branching, while they are sufficiently deformed by forming deformation bands.

The D3 alloy shows a stable crack growth as shown in Figures 6(b) and (c), which indicates the high resistance to crack growth. As shown in the *R*-curve of Figure 7, the stress intensity factor at the time of crack initiation of the D3 alloy is the same as that of the D1 or D2 alloy, but steadily increases with the increasing crack length, finally reaching 45 MPa$\sqrt{m}$ and showing the typical *R*-curve behavior. As a result of the occurrence of crack blunting or branching at the blocked sites of the crack, the higher stress intensity factor is required for the further crack propagation. The oval-shaped region in Figure 7 indicates the region of abrupt increase in stress intensity factor, which confirms that the crack blunting and branching are closely related with the abrupt increase in stress intensity factor. This *R*-curve shows the increasing resistance to crack growth according to the presence of dendrites. When considering the crack initiation and growth toughness and crack propagation behavior simultaneously, overall fracture properties of the D3 alloy are the best among the three alloys, although the crack initiation toughness values are similar because of their similar yield and tensile strengths. The ductility is also improved by the plastic deformation due to the formation of deformation bands (Table II).

Since the *in situ* fracture test is a good method to directly observe the effects of microstructural factors such as ductile dendrites and amorphous matrix on microfracture behavior, it can be effectively used to analyze the deformation and fracture behavior of Ti-based amorphous alloys. The current study confirms excellent fracture properties of the D3 alloy over the D1 or D2 alloy according to the observation of the microfracture, the *R*-curve behavior, and the fractographic observation, although the measured crack initiation toughness is almost the same in the three alloys. The improved resistance to crack growth is explained by the presence of ductile dendrites in terms of the mechanisms of (1) blocking of crack growth and crack blunting, (2) deformation band formation at dendrites, and (3) transition of fracture mode. Particularly in the D3 alloy, the wide and homogeneous formation of deformation bands at dendrites is observed because of the optimal size (63 μm) of dendrites, which offers the favorable feasibility in applications where amorphous alloys are required to possess excellent fracture properties.

V. CONCLUSIONS

Fracture properties of Ti-based amorphous alloys containing ductile β dendrites were evaluated, and the results were explained in relation to the direct observation of microfracture process.

1. The three Ti-based amorphous alloys modified from a Ti-6Al-4V alloy contained dendrites from 74 to 76 of vol pct, effective sizes of which varied from 63 to 104 μm. Their yield and tensile strengths were similar within the ranges from 1390 to 1440 and 1490 to 1510 MPa, respectively, and the tensile elongation increased in the order of the D1, D2, and D3 alloys to reach 7.1 pct in the D3 alloy.
2. According to the observation of microfracture processes of the D1 alloy containing coarse dendrites, a microcrack initiated at the amorphous matrix of the notch tip and propagated along the amorphous matrix, which led to abrupt crack growth and final fracture. In the D3 alloy containing fine dendrites, deformation bands initiated at dendrites near the notch tip, while a crack initiated along the amorphous matrix. The crack growth was frequently blocked by dendrites, and many deformation bands were formed near or in front of the propagating crack, thereby resulting in a zig-zag fracture path.
3. Since the crack initiation toughness measured from the *in situ* fracture test was heavily affected by the stress applied to the specimen at the time of crack initiation at the crack tip, the crack initiation toughness values were almost the same within the range from 35 to 36 MPa$\sqrt{m}$ within error ranges. However, according to the *R*-curve analysis data, the improvement of overall fracture properties in the D3 alloy was explained by the optimal effective size of dendrites in terms of mechanisms of blocking of crack growth and crack blunting, and formation of deformation bands at dendrites.

ACKNOWLEDGMENTS

This study was supported by the National Research Foundation of Korea (NRF) Grant (No. 2010-0026981) funded by the Ministry of Education, Science, and Technology, Korea, and by the Brain Korea 21 PLUS Project for Center for Creative Industrial Materials.

REFERENCES

1. W. Chen, Y. Wang, J. Qiang, and V. Dong: *Acta Mater.*, 2003, vol. 51, pp. 1899–1907.
2. H.A. Shivaee, A. Castellero, P. Rizzi, P. Tiberto, H.R.M. Hosseini, and M. Baricco: *Met. Mater. Int.*, 2013, vol. 19, pp. 643–49.
3. Y.C. Kim, J.M. Park, J.K. Lee, F.H. Bae, W.T. Kim, and D.H. Kim: *Mater. Sci. Eng.*, 2004, vols. A375–377, pp. 749–53.
4. R. Busch, A. Masuhr, and W.L. Johnson: *Mater. Sci. Eng.*, 2001, vols. A304–306, pp. 97–102.
5. J.M. Park, H.J. Chang, K.H. Han, W.T. Kim, and D.H. Kim: *Scripta Mater.*, 2005, vol. 53, pp. 1–6.
6. M. Taboosi, F. Karimzadeh, M.H. Enayati, S. Lee, and H.S. Kim: *Met. Mater. Int.*, 2013, vol. 19, pp. 901–06.
7. D.E. Polk and D. Turnbull: *Acta Metall.*, 1972, vol. 20, pp. 493–98.
8. C.A. Pampillow: *Scripta Metall.*, 1972, vol. 6, pp. 915–17.
9. T.E. Kim, S.W. Sohn, J.M. Park, C.W. Bang, W.T. Kim, and D.H. Kim: *Met. Mater. Int.*, 2013, vol. 19, pp. 667–71.
10. C.C. Hays, C.P. Kim, and W.L. Johnson: *Phys. Rev. Lett.*, 2000, vol. 84, pp. 2901–04.
11. C.C. Hays, W.L. Johnson, and C.P. Kim: *Mater. Sci. Eng.*, 2001, vols. A304–306, pp. 650–55.

12. D.C. Hofmann, J.-Y. Suh, A. Wiest, G. Duan, M.-L. Lind, M.D. Demetriou, and W.L. Johnson: *Nature*, 2008, vol. 451, pp. 1085–89.
13. Y.S. Oh, C.P. Kim, S. Lee, and N.J. Kim: *Acta Mater.*, 2011, vol. 59, pp. 7277–86.
14. D.J. Ha, C.P. Kim, and S. Lee: *Mater. Sci. Eng.*, 2012, vol. A552, pp. 404–09.
15. D.J. Ha, C.P. Kim, and S. Lee: *Mater. Sci. Eng.*, 2012, vol. A558, pp. 558–65.
16. D.L. Davison: *Metall. Trans.*, 1987, vol. 18A, pp. 2115–28.
17. J.G. Lee, D.-G. Lee, S. Lee, and N.J. Kim: *Metall. Mater. Trans.*, 2004, vol. 35A, pp. 3753–61.
18. S.R. Nutt and L.M. Duva: *Scripta Metall.*, 1986, vol. 20, pp. 1055–58.
19. M. Tavoosi, M.H. Enayati, and F. Karimzadeh: *Met. Mater. Inter.*, 2011, vol. 17, pp. 853–56.
20. D.C. Hofmann, J.-Y. Suh, A. Wiest, M.L. Lind, M.D. Demetriou, and W.L. Johnson: *Proc. Natl. Acad. Sci. USA*, 2008, vol. 105, pp. 20136–40.
21. C. Jeon, C.P. Kim, S.-H. Joo, H.S. Kim, and S. Lee: *Acta Mater.*, 2013, vol. 61, pp. 3012–26.
22. M.W. Lee, H.J. Shin, S.H. Hong, J.T. Kim, H. Choi-Yim, Y. Seo, W.H. Lee, P. Yu, M. Qian, J.K. Lee, and K.B. Kim: *Met. Mater. Int.*, 2014, vol. 20, pp. 1–5.
23. J.G. Lee, K.-S. Sohn, S. Lee, N.J. Kim, and C.P. Kim: *Mater. Sci. Eng.*, 2007, vol. A464, pp. 261–68.
24. C.-Y. Son, C.K. Kim, S.Y. Shin, and S. Lee: *Mater. Sci. Eng.*, 2009, vol. A508, pp. 15–22.
25. C. Jeon, C.P. Kim, and S. Lee: *Metall. Mater. Trans.*, 2012, vol. 43A, pp. 3675–86.
26. J.G. Lee, S.S. Park, D.-G. Lee, S. Lee, and N.J. Kim: *Intermetallics*, 2004, vol. 12, pp. 1125–31.
27. B. Kim, J. Do, S. Lee, and I. Park: *Mater. Sci. Eng.*, 2010, vol. A527, pp. 6745–57.
28. D.-G. Lee, S. Lee, and C.S. Lee: *Mater. Sci. Eng.*, 2004, vol. A366, pp. 25–37.
29. J.W. Qiao, J.T. Zhang, F. Jiang, Y. Zhang, P.K. Liaw, Y. Ren, and G.L. Chen: *Mater. Sci. Eng.*, 2010, vol. A527, pp. 7752–56.
30. S. Lee, K.-S. Sohn, C.G. Lee, and B.I. Jung: *Metall. Mater. Trans.*, 1997, vol. 28A, pp. 123–34.
31. J.J. Lewandowski, M. Shazly, and A. Shmimi Nouri: *Scripta Mater.*, 2006, vol. 54, pp. 337–41.
32. B. Gludovatz, S.E. Naleway, R.O. Ritchie, and J.J. Kruzic: *Acta Mater.*, 2014, vol. 70, pp. 198–207.
33. D. Broek: *Elementary Engineering Fracture Mechanics*, Martinus Nijhoff Publishers, Boston, 1982, pp. 297–309.